Supplementary Information

Towards the Rational Design of Pt-based Alloy Catalysts for the Low-Temperature Water-Gas Shift Reaction: from Extended Surfaces to Single Atom Alloy

Yuqi Yang[†], Tonghao Shen[†], Xin Xu*

Collaborative Innovation Center of Chemistry for Energy Materials, Shanghai, Key Laboratory of Molecular Catalysis and Innovative Materials, MOE Key Laboratory of Computational Physical Sciences, Department of Chemistry, Fudan University, Shanghai 200438, China

Email: xxchem@fudan.edu.cn

† These authors contributed equally to this work.

Table of Contents

S1. Details in energetic calculations.

S1.1. Parameters of DFT calculations on the Pt(111) surface.

Density functional theory (DFT) calculations were carried out by using the Vienna ab initio simulation package (VASP). [1,2] The electron-core interaction was described by the projector-augmented wave (PAW) scheme, while the electronic states were expanded on a plane wave basis with a cutoff of 400 eV for kinetic energy. [3,4] The electron exchange-correlation for all gaseous and surface species including adsorbates and transition states were treated by the Bayesian error estimation functional with van der Waals corrections (BEEF-vdw). [5] For some key energetic parameters such as the energy barrier of water dissociation, three other DFT functionals, including the Perdew-Burke-Ernzerhof (PBE) functional,[6] the extended Perdew-Burke-Ernzerhof (xPBE) functional[7] and the van der Waals Density Functional (vdW-DF),[8] were employed to confirm the results given by the BEEF-vdw functional.

The non-periodic calculations for gaseous species were performed in cubic supercells with the edge length of 10 Å, in order to eliminate the unphysical lateral interaction between neighboring supercells. All atoms in the non-periodic systems were completely relaxed during the geometrical optimizations. The Monkhorst-Pack grid for k-point was set to be (10×10×10). In terms of DFT calculations on extended surfaces, Pt(111) surfaces were described using a (3×3) slab model with four layers. Two bottommost layers were kept fixed, while two topmost layers and the adsorbates

were relaxed during geometrical optimizations. The calculated lattice constant of Pt bulk was found to be 3.924 Å, which is in good agreement with the experiment value of 3.92 Å. In this work, a (4×4×1) Monkhorst-Pack grid was applied to integrate the first Brillouin zone, and a 15 Å vacuum layer perpendicular to the surface slabs along the z-direction was adopted. The transition states (TS) were located by the Climbing-Image Nudged Elastic Band (CINEB) method and further confirmed in harmonic analysis by the existence of single imaginary frequency along the reaction coordinate.[9-11] The adsorbates and transition states were optimized until all forces were below 0.03eV.

S1.2. Structures of the Pt-alloys.

In this work, different PtM(M = Ag, Au, Co, Cu, Ir, Mo, Ni, Os, Pd, Re, Rh, Ru) alloys, including subsurface alloy structure (PtMPt), core-shell structure (M core-Pt shell, M-Pt), substrate core-shell structure Pt_3M-Pt, and surface alloy structure such as single atom alloy (SAA) with M_1@Pt, M_1@PtM'Pt structures, or surface cluster M_{1-n}@Pt structure (n = 1, 2 and 3), were employed to investigate the electronic and the synergetic effects, as shown in Figure S1. The lattice constants of different structures were determined by the major component metal, i.e. for subsurface alloys, substrate core-shell structures, and surface alloy structures, the lattice constants used were the same as that of the Pt metal, while for core-shell M-Pt structures, the lattice constants of core metal M were used, as listed in Table S1. The settings of DFT calculations used for Pt-alloys were the same as that on the Pt(111) surface.

S1.3. Zero point energy (ZPE) and entropy corrections.

The ZPE correction for each species was based on the harmonic oscillator approximation,

$$ZPE = \sum_i \frac{1}{2} h\nu_i \tag{S1}$$

where h is the Planck constant, and ν_i are the computed real frequencies.

The thermodynamic entropy corrections were also taken into account. For weakly bound molecular adsorbates such as H_2O, the adsorption entropy was evaluated by using the Campbell-Sellers equations,[12]

$$S_0^{ad}(T) = 0.70 S_0^{gas}(T) - 3.3R \tag{S2}$$

where $S_0^{gas}(T)$ is the entropy of species in gas phase, which is calculated by using the Shomate equation with parameters taken from the NIST chemistry web book, and R is the ideal gas constant.[13] The adsorption entropy of CO and the reaction entropy of every surface reaction were calculated based on the harmonic normal mode approximation,[14]

$$S_{vib} = R \sum_i \left[\frac{x_i}{e^{x_i} - 1} - \ln(1 - e^{-x_i}) \right] \tag{S3a}$$

$$x_i = \frac{h\nu_i}{k_B T} \tag{S3b}$$

where k_B is the Boltzmann constant. It is known that for the soft modes with low frequencies, the anharmonic effects are important and the harmonic approach often fails. Therefore, the imaginary and the low frequency modes ($\nu_i < 100$ cm^{-1}) were

truncated during the entropy correction, as used in our previous work.[15]

S1.4. The dissociative adsorption of H_2O.

In the investigations when the adsorbate-adsorbate interactions were ignored,[16, 17] H_2O molecule was usually assumed to adsorb on the surface from the gaseous phase first, and then dissociate with two adjacent empty sites, as indicated in Equations S4-S5.

$$H_2O(g) + * \rightleftharpoons H_2O^* \qquad (S4)$$

$$H_2O * + * \rightleftharpoons OH^* + H^* \qquad (S5)$$

However, in our DFT calculations, we found that the adsorbed H_2O molecule is unstable when getting close to adsorbed CO molecule. This is particularly true when CO coverage is higher than 1/3 ML. As shown in Table S2, the length of Pt-O bond in the adsorbed H_2O becomes larger with the increase of CO coverage, which suggests that the repulsion of neighboring CO makes H_2O hard to adsorb on the Pt(111) surface. To get a correct description of the influence of CO coverage on H_2O adsorption, in the present work, we assumed that a gaseous H_2O molecule dissociatively adsorbs on a couple of neighboring empty sites (Equation 2 in the main text) with a transition state identical to that in H_2O dissociation (equation S5). In fact, under the assumption that the adsorption and desorption of H_2O (equation S4) is in equilibrium, which is the case in the LT-WGS reaction, these two assumptions should be the same, while ignoring the adsorbate-adsorbate interactions. Here we performed KMC simulations

in different regions on the activity map, in which the interaction between H_2O^* and CO^* was set to zero, to illustrate the accuracy of our assumption. The data are summarized in Table S3. It can be seen that the TOF calculated by the two models are numerically identical for the four corners and the central point on the activity map. Therefore, it is expected that the dissociative adsorption assumption is well suited for describing the kinetics of the LT-WGS reaction, at least in the region that we are interested in the present work.

S1.5. Adsorbate-adsorbate interactions among surface species.

The repulsive interactions among surface species usually influence the kinetic behaviors by affecting the coverages of surface species and the energy barriers. In the Pt-based LT-WGS reaction, CO^* was the major surface species. Thus, we considered the adsorbate-adsorbate interactions of the first nearest neighbor sites (1NN) involving CO^*, while neglected the interactions among other species. The parameters of adsorbate-adsorbate interactions between CO and each surface species (adsorbates and transition states) are summarized in Table S4.

S1.6. The re-adsorption of products.

Under the LT-WGS reaction condition, the partial pressures of the products (CO_2 and H_2) are considerably lower than the reactants (CO and H_2O), therefore, the re-adsorptions of the products are so slow that their contributions to the reaction rate are usually ignored in the literature.[18, 19] To evaluate the error of this approximation,

we have performed KMC simulations that included the re-adsorption of the products on Pt(111) surfaces at 400 K. The partial pressure of CO, H_2O, CO_2 and H_2 were 0.032, 0.075, 0.01, and 0.01 bar, respectively. The resulting TOF is 1.34 s^{-1} $site^{-1}$, which is very close to the value 1.37 s^{-1} $site^{-1}$ without considering the re-adsorption of the products. These calculations have shown that ignoring the re-adsorption of the products is a good approximation in the investigation of the LT-WGS reaction, and we have adopted this approximation in the present work. Also other side reactions that using the products (CO_2 and H_2) as the reactants should not be significant.

S2. Details in kinetic simulations.

S2.1. KMC simulations.

After getting necessary energetic parameters, the kinetic evolutions under different temperatures were obtained by carrying out KMC simulations using the algorithm as implemented in the XPK program.[20] The Pt(111) surface, as well as the Pt subsurface alloys, was modeled by a well-defined 100×100 hexagonal lattice grid with periodic boundary conditions, while for Pt alloys with promoter atom on the surface, the surface model of a 30×30 hexagonal lattice grid including one promoter atom site and 899 host atom sites was employed. For simplicity, the KMC simulations were carried out based on the definition of a coarse-grained site, i.e. each surface intermediate could only occupy its most stable adsorption site (top, bridge, or hollow sites) correlated to a surface atom; and once a site was occupied, this atom was occupied, and the other correlated sites were not able to be taken due to the repulsive interactions between intermediates.

In the KMC simulations, the time average of a kinetic property was taken as its expectation value. For instance, the coverage expectation of CO* on a specific site x can be calculated by the following equation,

$$\theta_{CO^*}^x = \frac{\sum_i^{n_{step}} o_{CO^*}^x \delta t_i}{\sum_i^{n_{step}} \delta t_i} \tag{S6}$$

where the subscript i runs over all the snapshots of the trajectory, $o_{CO^*}^x$ is the occupation number of CO* on the site x, which can be either 1 (if the site x is

occupied by CO*) or 0 (if the site x is not occupied by CO*), and δt_i is the time interval of the i-th snapshot, which is given by,

$$\delta t_i = -\frac{\ln R_N}{k_{tot}} \tag{S7}$$

in which R_N is a random number between 0 and 1, and k_{tot} is the sum of the reaction rate constants of all possible surface reactions of i-th snapshot. In the present work we did not distinguish different surface atoms of an element, e.g. all the Pt atoms are considered to be identical, and therefore, the coverage of a surface intermediate on an element is the average of all the surface atoms of this element.

$$\theta_{CO^*}^{Pt} = \frac{\sum_x^{n_{Pt}} \theta_{CO^*}^x}{n_{Pt}} \tag{S8}$$

In the investigation of kinetics of the LT-WGS reaction, KMC simulations were performed at 400 K to obtain the activity map. The partial pressures of CO, H_2O were set to be 0.032 bar and 0.075 bar, respectively, while the partial pressures of CO_2 and H_2 were set to be zero. These parameters were in consistency with the experimental setting reported by Duke et al.[21] Furthermore, to validate the setting and calculations in our model, KMC simulations were performed on the Pt(111) surface. The apparent activation energy was obtained by an Arrhenius plot in the temperature range of 525 K to 675 K. The partial pressures for the gaseous CO and H_2O were set as 0.020 bar and 0.033 bar, respectively, while the partial pressures of CO_2 and H_2 were zero.[22]

It is well known that the rate of adsorption and desorption processes are much higher than other kinetically-relevant reactions, which may cause the problem of time

scale separation.[20] In this work, we scaled down the rate coefficient of adsorption and desorption processes in proportion without changing the thermodynamics properties, to make the reaction rate for adsorption and desorption processes 100 to 1000 times larger than the other elementary reactions.

S2.2. Mean-field microkinetic simulations.

The activity map calculated by mean-field microkinetic model (MF-MKM) was also involved in this work as a comparison. The solutions of MF-MKM without adsorbate-adsorbate interactions were mainly performed by using the Newton iteration method (NIM) in the XPK program. In addition, reversibility iteration method (RIM) was also employed to obtain the initial guess of the adsorbate coverages,[23] as RIM provides a powerful and convenient way to circumvent the notorious problem of "stiffness" in the microkinetic modeling. To compare the kinetic results of MF-MKM and KMC simulations, the energetic settings and reaction conditions in MF-MKM were set to be the same as that in KMC simulations.

S3. Thermodynamics in the WGS reaction.

S3.1. Thermodynamic corrections and Gibbs free energy profile.

As described in section S1.3, the ZPE and the thermodynamic entropy corrections were included in the thermodynamic parameters in the present work. The ZPE corrections on the reaction heats and energy barriers for the elementary steps on the Pt(111) surface are shown in Table S5, while the entropy corrections, i.e. $-T\Delta S$ at 400 K, are summarized in Table S6. It could be seen that the reaction heats, as well as the energy barriers, are insensitive to the ZPE corrections. On the other hand, the entropy corrections significantly influence the energetic parameters in adsorption/desorption processes involving gaseous species such as CO and H_2O, while the entropy effects on the surface reaction is also not small. For desorption of H_2 and CO_2, the partial pressures were set to be zero, which led to a negative infinity free energy. Therefore, the thermodynamic corrections of these two steps were not taken into account.

The Gibbs free energy profile of LT-WGS on the Pt(111) surface is plotted in Figure S2. At 400 K, CO adsorption is exothermic with a Gibbs free energy of -0.81 eV. The dissociative adsorption of H_2O is endothermic with a Gibbs free energy of 0.82 eV and a free energy barrier of 1.20 eV. The formation of COOH* is slightly endothermic with a Gibbs free energy of 0.05 eV, followed by the COOH* decomposition with a Gibbs free energy of -0.05 eV. The free energy barriers of COOH* formation and decomposition are 0.48 eV and 0.60 eV, respectively. For desorption processes of H_2 and CO_2, the Gibbs free energy of desorption process are

negative infinity. For the simplicity, we assumed that the ZPE and entropy corrections are identical on the surfaces of different alloys.

S3.2. Effects of CO adsorbate-adsorbate interactions.

Under reaction conditions of LT-WGS, CO is the major surface species on Pt(111). A high CO coverage obviously affects the thermodynamic properties by adsorbate-adsorbate interactions. The results of the BEEF-vdw functional are shown in Figure 1b in the main text. It is known that as the CO coverage increases, the CO binding affinity (i.e., the magnitude of E_{CO*}) decreases, while the energy barrier of RDS (i.e., $E_a(RDS)$) increases. To confirm our observations on BEEF-vdw, three different density functionals, PBE, vdW-DF and xPBE, were used to calculate E_{CO*} and $E_a(RDS)$ at different CO coverages. The results are summarized in Table S7. It can be seen that four density functionals provided the same trends of CO coverage effects on E_{CO*} and $E_a(RDS)$, which confirmed our results based on the BEEF-vdw functional. By comparing the results of four density functionals, it is found that the slopes calculated by PBE and xPBE are larger than those by BEEF-vdw and vdw-DF. It is expected that the CO interactions may play a role, which is more important in the computations of PBE and xPBE than that in the BEEF-vdw and vdw-DF calculations.

S3.3. Details in building linear scaling relationships.

In this work, we fitted the linear scaling relationships of thermodynamic parameters with the linear combination of E_{CO*} and E_{OH*} on nine subsurface alloys

(PtMPt(111), M = Ag, Au, Cu, Ir, Os, Pd, Pt, Rh, Ru). As pointed out above, different

subsurface metals were assumed to only modify the electronic energies of surface Pt

atoms, while the ZPE and the thermodynamic corrections were kept the same as that

on the Pt(111) surface. The results of surface intermediates and transition states were

indicated in Figure 1d and Figure 1e in the main text and the corresponding

fitting parameters and the statistic deviations were provided in Table S8 and Table S9,

respectively.

S4. Details in the construction of the activity map.

S4.1. Activity map via KMC simulations.

Coverage is an important property in understanding the reaction kinetics. For the LT-WGS reaction, CO is the major species on the Pt-alloy surfaces due to its high adsorption energy, which determines the coverages of the other surface species and further affects the energetic parameters of the elementary reactions through adsorbate-adsorbate interactions. To illustrate the fact that the catalyst surface is dominated by adsorbed CO, we plotted the coverages of each surface intermediate verses E_{CO*}, while E_{OH*} is fixed at 0.80 eV, which is close to the value on the Pt(111) surface. The results are shown in Figure S3a. It can be seen that, in the range of E_{CO*} involved in the present work, the CO* is the major adsorbed species, while coverages of all other surface intermediates are considerably lower than that of CO*. As the CO binding affinity decreases from -1.80 eV to -0.80 eV, the CO coverage decreases from about 0.66 ML to about 0.20 ML, while the coverage of the empty site increases, accordingly. There are two steps on the coverage curve; the first one appears in the range that E_{CO*} varies from -1.80 eV to -1.60 eV, where the CO coverage is about 0.66 ML, while the second one appears in the range that E_{CO*} varies from -1.30 eV to -0.90 eV, where the CO coverage is about 0.33 ML. As shown in Figure S3b, these two values correspond to two kinetically stable "phases" on the hexagonal lattice, i.e., the 1/3 ML coverage corresponds to the phase without the first nearest neighboring (1NN) CO-CO interaction and the 2/3 ML coverage corresponds to the phase with

15

three 1NN CO-CO repulsions on each adsorbed CO. In the ranges of these stable phases, the CO coverage is insensitive to the change of E_{CO*}. On the other hand, during the phase transition in the region that E_{CO*} between -1.60 and -1.30 eV, the CO coverage becomes highly sensitive to E_{CO*}. The CO coverage dependence on E_{CO*} caused by phase transition explains the coverage effects on the energy barrier of the RDS, as displayed by the dark cyan line in Figure 2c in the main text.

Spatial correlation of the empty sites plays an important role in reaction kinetic.[24] It is known that the RDS requires two neighboring empty sites; therefore, the spatial correlation of the empty sites can significantly affect the reaction kinetics. To illustrate the effect of the spatial correlation, we compared the number of neighboring empty sites accounted in KMC (N_{pair}^{KMC}) simulations and that evaluated by mean field approximation (N_{pair}^{MF}) based on the coverage of the empty sites given in KMC simulations. The logarithmic numbers of neighboring empty sites versus E_{CO*} with a fixed E_{OH*} at 0.80 eV are plotted in Figure S4. The mean field approximation assumes a well-mixed catalyst surface in the diffusion limit, which leads to an estimation of $N_{pair}^{MF} = N * \theta_* * \theta_*$, where N indicates the total number of active sites. It can be seen that, the KMC result agrees well with that in the mean field approximation in the low CO adsorption energy region between -0.80 eV to -1.50 eV. Further increasing the CO binding affinity to -1.80 eV results in a significant deviation of the mean field approximation from the KMC simulation results. This observation can be understood from the transition between two stable phases shown in Figure S3b. It can be seen that in the 1/3 phase, all the adsorbed CO are separated by

16

empty sites and there are enough pair of empty sites such that the mean field approach is approximately correct, while in the 2/3 ML phase, there are no neighboring empty sites at all and the mean field approximation totally fails.

It is worthy to note that the CO adsorption energy on the Pt(111) surface is -1.46 eV in the BEEF-vdW calculation, which is close to the marker at which the mean field approximation tends to collapse. As a result, in the region we are interested, i.e. the CO binding affinity is similar or lower than that on the Pt metal, the spatial correlation does not strongly affect the reaction kinetics and the reaction kinetics can be totally understood from the energy barrier of the RDS, while in the region where CO binding affinity is much higher than that on the Pt(111) surface, the mean field approach fails and the spatial correlation can dominate the reaction kinetics, as we have seen in Figure 2 in the main text. We would like to emphasize that this conclusion is strongly dependent on the DFT calculations of CO adsorption energy, i.e. the location of Pt on the activity map, which highlights the significance of an accurate estimation of the key thermodynamic parameters in the catalyst design.

S4.2. Activity map via MF-MKM without adsorbate-adsorbate interactions.

In MF-MKM, the missing of adsorbate-adsorbate interactions can significantly overestimate the influence of $E_{\text{CO}*}$ on the reaction kinetics. We performed the MF-MKM simulations to evaluate the reaction rate and the coverages of surface species on the basis of thermodynamic parameters which are the same as those used in KMC simulations. As shown in Figure S5b, the logarithmic coverage of the empty

sites linearly increases as the CO binding affinity increases. The lack of CO-CO repulsion results in an unphysically severe poison of CO* in the range of E_{CO*} from -1.80 eV to -0.90 eV, which covers almost all the interested region in the present work. As E_{CO*} changes from -1.80 eV to -0.80 eV, the empty site coverage calculated by MF-MKM increases from 1.01×10^{-13} ML to 2.87×10^{-1} ML, while the corresponding KMC results change from 0.33 ML to 0.81 ML. The dramatic change for the coverage of the empty sites in MF-MKM is responsible for its overestimation of the effects of E_{CO*} as compared to those based on the KMC simulations, which, in turn, leads to a wrong direction for the rational design of new catalysts. It is worthy to note that the adsorbate-adsorbate interactions can be approximately considered in some advanced MF-MKM methods developed recently,[25-27] such that a reasonable CO coverage might be obtained. However, the spatial correlation between adsorbates, which plays an important role in the reaction kinetics, is still difficult to be described by the mean-field approximation. Therefore, it remains a challenge to describe the reaction kinetics on a poisoned catalyst surface using MF-MKM.

S5. Details in catalyst screening.

S5.1. The adsorption configurations of CO* and OH*

Figure S6 shows the most stable adsorption configurations of CO* and OH* on different metal/alloy surfaces. According to the BEEF-vdW calculations, the CO* intermediate prefers to adsorb on the hollow sites on the Pt and PtCuPt surfaces, while on the PtRePt, RePt and Ru1-3@Pt alloys, the top sites are the most stable ones. The OH* intermediate prefers the bridge sites on Pt surfaces, while it prefers the top sites on the surfaces of alloy catalysts.

It can be seen that, the most stable adsorption site of CO* on Pt(111) surfaces is the hollow site, instead of the top site observed in the experiments,[28] which is the well-known "CO-puzzle" for GGA functionals.[29] Despite the BEEF-vdW functional does not correctly predict the relative stabilities of the top and the hollow sites, the adsorption energies on these two sites are very similar, i.e. the adsorption of CO on the hollow site is only -0.09 eV more stable than that on the top site. More importantly, the BEEF-vdW functional gives a good prediction of the CO adsorption energy on the most stable site (-1.46 eV) as compared to the experimental data (-1.43 eV).[28] As described in S2.1, a coarse-grained model was employed in the KMC simulations such that each surface intermediate could only occupy its most stable adsorption site; and once a site (either top, or bridge, or hollow) was occupied, the other correlated sites were not able to be taken due to the repulsive interactions between intermediates. Hence, the key parameters in the catalyst screening are the CO binding affinity and

the OH binding affinity, while the KMC results are not affected by the details of the adsorption sites.[16]

S5.2. Activity of the PtRePt subsurface alloy.

According to the activity map in Figure 2a in the main text, PtRePt is a good candidate catalyst for LT-WGS reaction due to its high OH binding affinity and low CO binding affinity as compared to the Pt(111) surface. To verify this prediction based on linear scaling relationship, we carried out KMC simulations based on the energetic data directly obtained by DFT calculations, as shown in Table S11. For PtRe Pt, the $E_a(RDS)$ of PtRePt calculated by DFT is 0.26 eV higher than that obtained by linear scaling relationship, while the $E_a(RDS)$ of Pt in DFT calculation is 0.10 eV lower than the linear scaling relationship results. The accumulation of error in $E_a(RDS)$, unfortunately, changed the relative activity of PtRePt as compared to that of Pt. The DFT-based KMC simulations showed that the TOF of PtRePt is about 0.3-fold lower than that of Pt, which suggests that PtRePt is actually not a satisfactory candidate catalyst.

S5.3. Activity of Cu$_1$@Pt and Cu$_1$@PtCuPt.

As discussed in the main text, the PtCuPt alloy is much less active than bulk Pt. However, one may be interested in the activity of surface Cu atom on the Pt catalyst, to investigate the activity of the PtCu alloy might be synthesized in some experiments.[30] The most favorable adsorption site for CO around the single surface

Cu atom was found to be the hollow site constructed by a Cu atom and two neighboring Pt atoms. It is known that the CO binding affinity on Pt is much higher than that on Cu; therefore, the adsorbed CO molecule is much closer to the Pt atoms than to the Cu atom, as shown in Figure S7. In comparison, the OH species locates at almost the middle point of the hollow site between Cu and Pt atoms in its most stable configuration. In the coarse graining model, all these sites belong to the Cu atom, and the occupation on one of them would prevent the occupation on its neighboring sites, which is reasonable for the real surfaces. In this manner, the exposure of the Cu promoter on surfaces increases E_{CO*} and E_{OH*} for both alloys of $Cu_1@Pt$ and $Cu_1@PtCuPt$, as compared to the host surface Pt.

As shown in Figure 3a and Figure 3b in the main text, the exposure of the Cu promoter on surfaces enhances the activity of the host Pt and PtCuPt by 1.29 and 3.41 orders of magnitude, respectively. To verify the activity of $Cu_1@Pt$ and $Cu_1@PtCuPt$ predicted by using linear scaling relationship, additional DFT calculations were performed to compute the CO adsorption energy and the energy barrier of the RDS. The DFT-based results are summarized in Table S12. Unfortunately, although the surface Cu atom increases the adsorption energy of OH, the energy barriers of the RDS on both $Cu_1@Pt$ and $Cu_1@PtCuPt$ are higher than that on Pt and PtCuPt, respectively. Using the energetic data directly from DFT calculations, the followed KMC simulations also suggested that the TOF of the Cu promoters are lower than the corresponding values of the host metal or alloys. Finally we arrived at the conclusion that the performance of the Pt catalyst can hardly be improved by alloying Cu as

SAA.

S5.4. Enhance the activity of the Ru₁@Pt alloys.

For Ru₁@Pt, although a stronger OH binding affinity reduces the energy barrier

of the RDS, a higher CO binding affinity, nevertheless, leads to a specific CO poison

on the Ru atom, and the improvement of the activity by Ru₁@Pt is limited as

compared to the bulk Pt. It is expected that this specific poison on the Ru atom can be

alleviated by changing its chemical environment. A straightforward way is to modify

the atoms in the subsurface. We screened different Ru₁Pt@PtMPt (M = Ag, Au, Cu, Ir,

Os, Pd, Re, Rh and Ru) alloys by energetic descriptors E_{OH*} and E_{CO*}, as shown in

Table S13. It could be seen that the CO binding affinity on the Ru promoter for

Ru₁Pt@PtRuPt, Ru₁Pt@PtOsPt and Ru₁Pt@PtRePt are much lower than that for

Ru₁Pt@Pt, while their OH binding affinities are similar. However, these subsurface

alloys also reduced the CO binding affinity on the neighboring Pt surface site

simultaneously, hence the averaged difference between E_{CO*}^{Ru} and E_{CO*}^{Pt} can still be

as large as 0.52 eV. As a result, the substitution of all Pt atoms in the subsurface by a

transition metal does not cure the specific CO poison. This observation was confirmed

by additional DFT calculations and KMC simulations, the results are summarized in

Table S14. It can be seen that the modification of metals in the whole subsurface does

not improve the activity of Ru₁@Pt.

Because the subsurface atoms simultaneously decrease the CO binding affinity on

both the promoter Ru and the host Pt, it is necessary to create a non-uniform local

chemical environment around the promoter Ru to break down the scaling relationship. As discussed in the main text, this target can be achieved by introducing Ru clusters embedded in Pt catalyst, and both the surface $Ru_x@Pt$ and the subsurface clusters $Ru_{1-x}@Pt$ exhibit much higher activity than the bulk Pt. The activities of these alloys are confirmed by explicit DFT and KMC simulations, as summarized in Table S15. It is clear that the CO binding affinity on the Ru promoter decreases as the number of the neighboring Ru atoms in the subsurface increases, i.e. the CO binding affinity on the surface Ru decreases from -1.87 eV in $Ru_1@Pt$ to -1.50 eV in $Ru_{1-3}@Pt$ alloy, which is very close to that on the Pt(111) surface, -1.46 eV. As a result, the coverage of the empty site increases from 5.67×10^{-6} to 1.07×10^{-1}, and the TOF increases from 3.0×10^{-4} to 1.5 $site^{-1}$ s^{-1}. On the other hand, the appearance of the neighboring surface Ru atoms also increases the coverage of the empty site, although they do not affect the CO adsorption energy. The strong 1NN CO-CO repulsion prevents the CO occupation of all neighboring surface Ru atoms, therefore, the coverage of the empty site on the $Ru_3@Pt$ alloy increases by about three orders of magnitude as compared to the $Ru_1@Pt$ alloy, which leads to a 73-fold increase of the TOF. On the basis of these observations, we concluded that small Ru clusters embedded in the Pt catalyst would effectively improve the catalytic performance for the LT-WGS reaction.

S5.5. Stability of the RuPt alloys.

The stability of the catalyst, which determines the experimental availability and applicability of the designed catalyst, is a key factor in catalyst design and screening.

We showed that agglomeration of Ru atoms on the surface and/or in the subsurface of the Pt catalyst could significantly enhance the activity of the bulk Pt, and picked up a number of candidates. These candidates are expected to be promising catalysts for the LT-WGS reaction if they are energetically feasible. As suggested in literature,[31] we took the formation energy ΔE (Equation S9) as a criterion to evaluate the stability of an alloy,

$$\Delta E = \frac{1}{n}\left(E_{alloy} - E_{Pt(111)} + nE_{1Pt} - nE_{1Ru}\right) \qquad (S9)$$

where n is the total number of Ru atoms in a RuPt alloy, E_{alloy} is the energy of the PtRu alloy in DFT calculations, $E_{Pt(111)}$ is the energy of the Pt(111) surface, E_{1Pt} and E_{1Ru} are energies of one Pt atom or Ru atom in the bulk. The results of ΔE are listed in Table S16. It can be seen that a Ru atom located in the subsurface is 0.61 eV more stable than that exposed on the surface, and the agglomeration of Ru atoms in the subsurface is favorable in terms of the formation energy as compared to the separated Ru atoms, which is in consistency with the observations reported in literature[31]. Therefore, we expected that the Ru clusters embedded in bulk Pt with a small portion of Ru atoms exposed on the surface is favorable in energy. In detail, the surface alloys $Ru_x@Pt$ (x = 1, 2 and 3) are energetically unstable as compare to the bulk Pt, while the cluster alloys $Ru_{1-x}@Pt$ (x = 1, 2 and 3) are much more stable, and the formation energy of $Ru_{1-3}@Pt$ alloy is only 0.08 eV as compared to the bulk Pt.
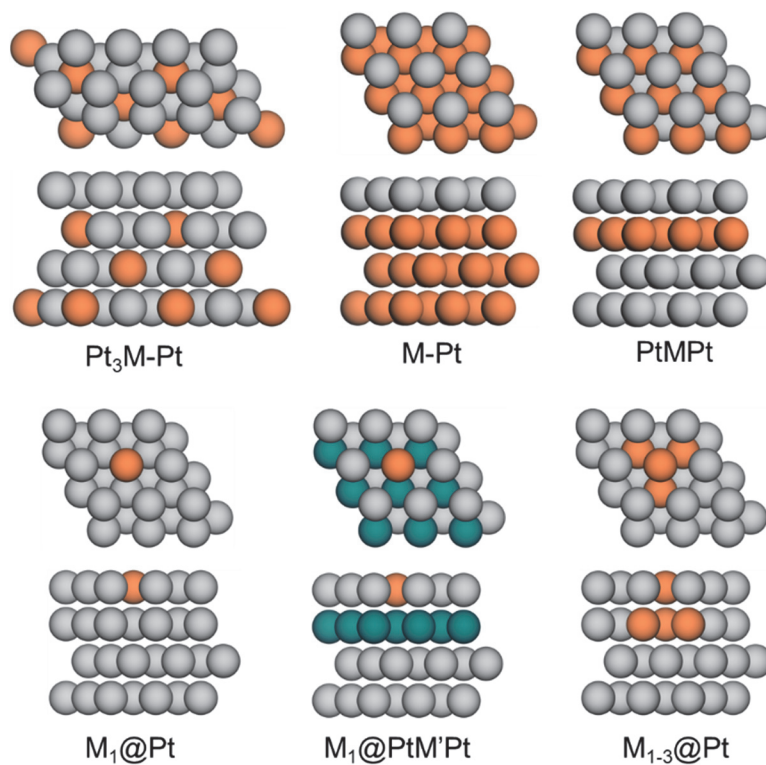
Figure S1. Structures of different Pt-alloys. Grey balls represent Pt atoms; while orange and green balls represent alloying metals M and M', respectively.
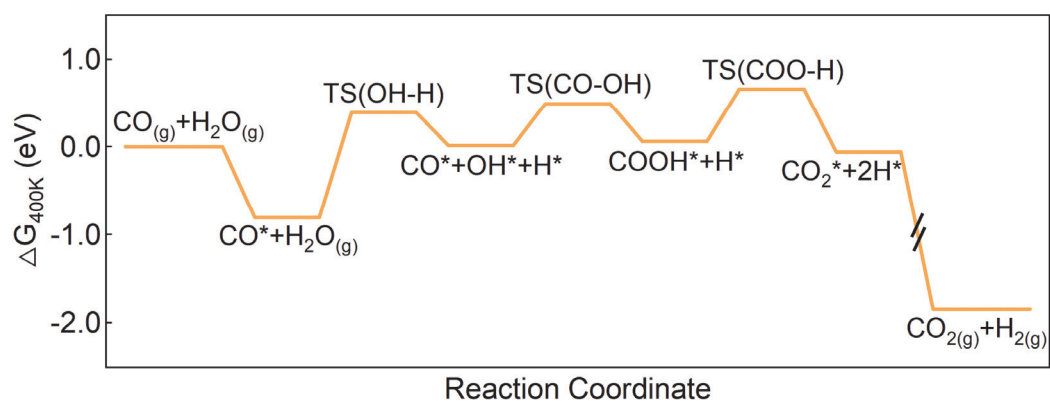
Figure S2. Gibbs free energy profile on Pt(111) at 400 K.
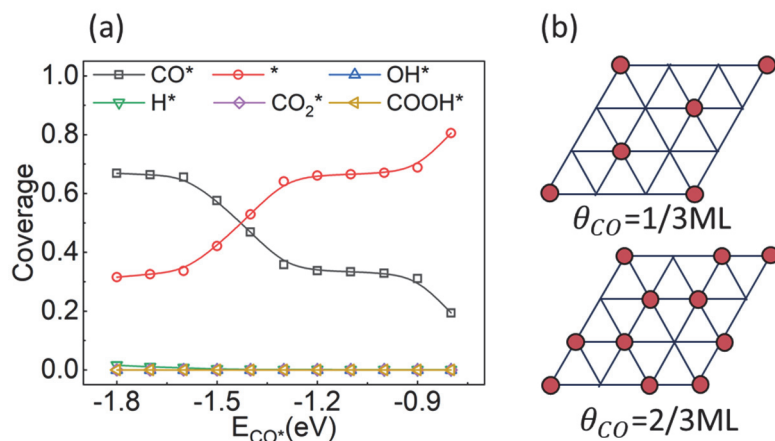
Figure S3. (a) Coverages of each surface species along E_{CO*} when E_{OH*} = 0.80 eV. All data points were calculated by KMC simulations. (b) Patterns of CO* at 1/3 and 2/3 ML, respectively.
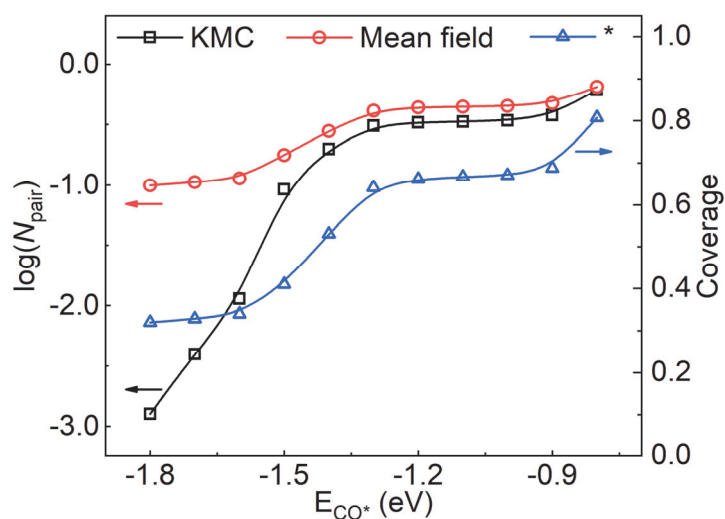
Figure S4. Number of the neighboring empty sites (N_{pair}) counted in KMC simulations (black square) and calculated by the mean-field approximation (red circle) using the coverage of the empty site obtained in KMC simulations (blue triangle). The grey dash line corresponds to E_{CO*} of Pt(111).
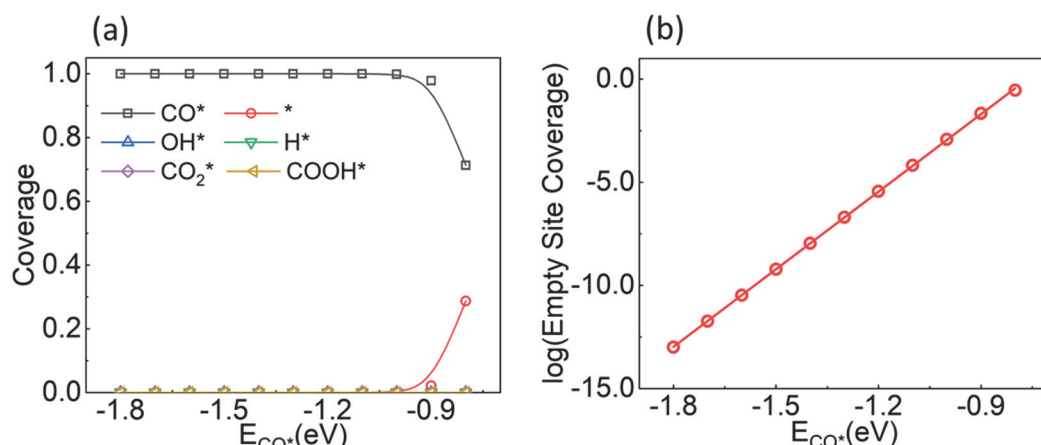
Figure S5. MF-MKM calculations of (a) coverages of surface species versus E_{CO*}; (b) the logarithmic coverage of the empty site versus E_{CO*} when E_{OH*} = 0.80 eV.
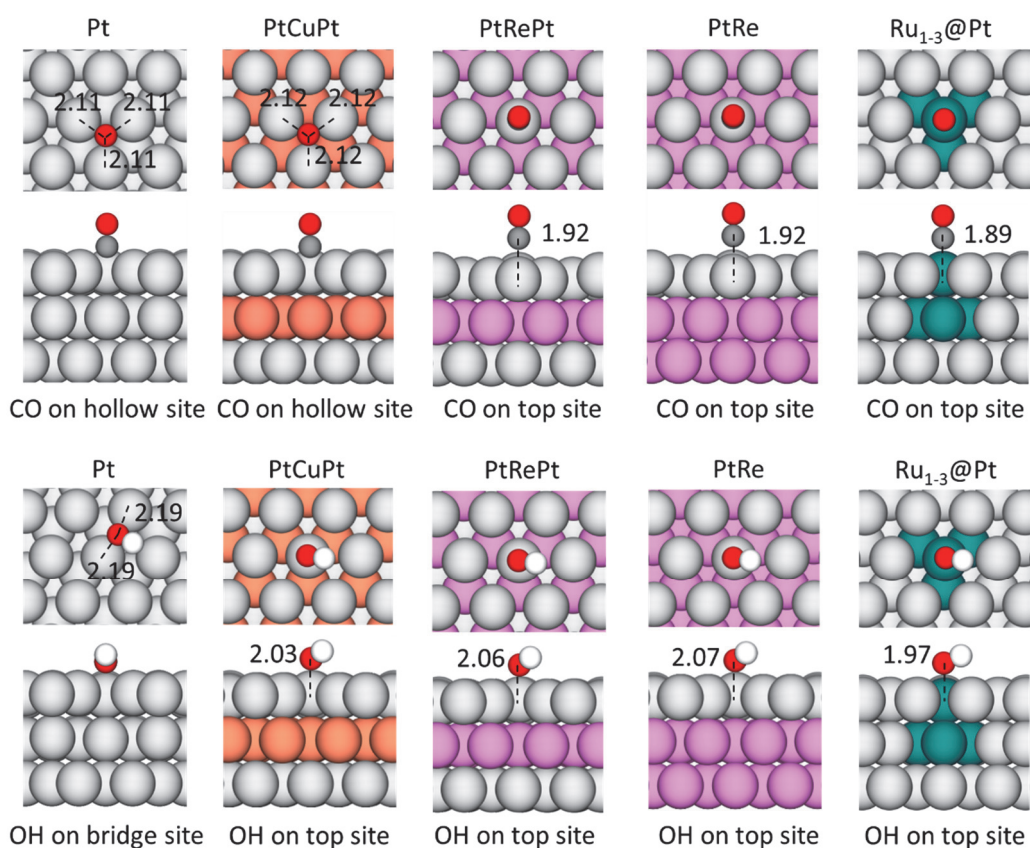
Figure S6. The adsorption configurations of CO* and OH* on different metal/alloy surfaces. The white, gray and red balls denote H, C, and O, respectively, while the silver, orange, pink and dark cyan balls present Pt, Cu, Re and Ru, respectively.
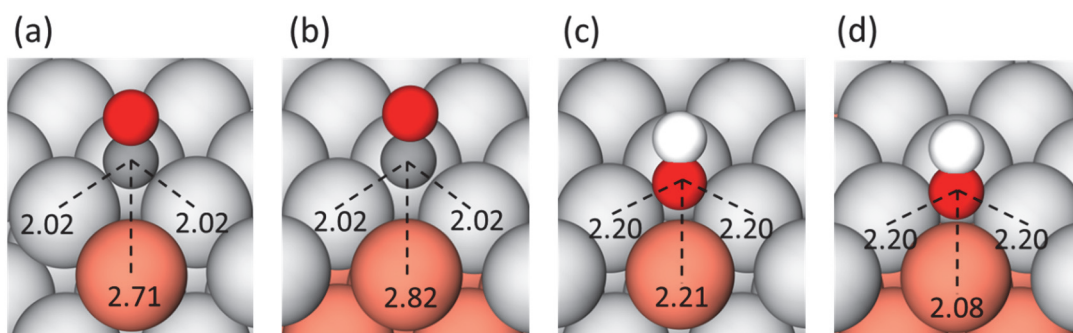
Figure S7. The most favorable adsorption site of CO (a-b) and OH (c-d) around a single surface Cu atom in $Cu_1@Pt$ (a and c) and $Cu_1@PtCuPt$ (b and d). The white, grey and red balls represent H, C and O, respectively, while the silver and orange balls represent Pt and Cu, respectively. The distances between adsorbates and metal atoms are given.

Table S1. Lattice constants for the core-shell M-Pt(111) structures

Structure name	Lattice constants (Å)
Ag-Pt(111)	4.086
Au-Pt(111)	4.078
Ir-Pt(111)	3.839
Mo-Pt(111)	3.147
Pd-Pt(111)	3.891
Re-Pt(111)	3.903
Rh-Pt(111)	3.804
Ru-Pt(111)	3.827

Table S2. DFT calculated Pt-O bond length for H_2O adsorbed on the Pt(111) surface at different CO coverage (θ_{CO}).

Density functionals	Pt-O bond length (Å)			
	$\theta_{CO} = 0$	$\theta_{CO} = 1/9$	$\theta_{CO} = 2/9$	$\theta_{CO} = 1/3$
BEEF-vdw	2.59	2.79	3.33	3.64
PBE	2.40	2.56	2.92	3.67
vdw-DF	2.63	2.91	3.29	3.61
xPBE	2.40	2.76	3.39	3.67

Table S3. The TOF calculated via the direct H_2O adsorption mechanism and the dissociative H_2O adsorption mechanism for different E_{CO*} and E_{OH*}. To apply the direct H_2O adsorption mechanism, the CO-H_2O interactions are ignored in these simulations.

		TOF	
E_{CO*}	E_{OH*}	H_2O direct adsorption	H_2O dissociative adsorption
-0.90	1.00	7.95×10^{-11}	7.98×10^{-11}
-0.90	0.20	2.54×10^{-1}	2.46×10^{-1}
-1.30	0.60	8.41×10^{-6}	8.52×10^{-6}
-1.70	1.00	3.08×10^{-12}	3.15×10^{-12}
-1.70	0.20	1.29×10^{-2}	1.16×10^{-2}

Table S4. Repulsive interaction energies for surface intermediates and transition states that involve CO*.

Surface intermediate/ transition state	CO-adsorbate repulsions (eV)
CO*	0.11
COOH*	0.10
OH*	0.04
H*	0.00
TS(OH-H)	0.05
TS(CO-OH)	0.12
TS(COO-H)	0.08

Table S5. ZPE correction of energetic parameters in each elementary reaction (eV).

Reaction	ΔE	E_a
$CO(g) + * \leftrightarrows CO*$	0.06	/
$H_2O(g) + * + * \leftrightarrows H* + OH*$	-0.03	-0.01
$CO* + OH* \leftrightarrows COOH* + *$	0.08	0.01
$COOH* + * \leftrightarrows CO_2* + H*$	-0.12	-0.19
$H* + H* \leftrightarrows H_2(g) + * + *$	-0.11	/
$CO_2* \leftrightarrows CO_2(g) + *$	0.00	/

Table S6. Entropy correction ($-T\Delta S$, T=400K) of each elementary reaction (eV).

Reaction	Entropy correction ($-T\Delta S$)	
	ΔE	E_a
$CO(g) + * \leftrightarrows CO*$	0.65	/
$H_2O(g) + * + * \leftrightarrows H* + OH*$	0.27	0.37
$CO* + OH* \leftrightarrows COOH* + *$	0.23	0.11
$COOH* + * \leftrightarrows CO_2* + H*$	0.07	0.01

Table S7. Effects of CO coverages on the CO binding energy (E_{CO}) and the energy barrier of the RDS ($E_a(RDS)$)

Property	Density functional	Energy at different CO Coverages (eV)				
		0	1/3	4/9	5/9	2/3
E_{CO}	BEEF-vdw	-1.46	-1.41	-1.36	-1.28	-1.19
	PBE	-1.76	-1.70	-1.61	-1.51	-1.40
	vdw-DF	-1.29	-1.25	-1.21	-1.14	-1.06
	xPBE	-1.54	-1.47	-1.41	-1.30	-1.16
$E_a(RDS)$	BEEF-vdw	0.83	0.91	1.12	1.14	1.15
	PBE	0.57	0.72	0.94	0.97	0.99
	vdw-DF	0.75	0.84	1.05	1.08	1.07
	xPBE	0.82	0.98	1.22	1.26	1.27

Table S8. Parameters and results of linear scaling relationships for reaction energies, $\Delta E_i = a(xE_{CO*} + yE_{OH*}) + b$.

Reaction	x	y	a	b	R^2	MAE
$H_2O(g) + * + * \leftrightarrows H* + OH*$	0.23	1.00	0.87	0.24	0.92	0.04
$CO* + OH* \leftrightarrows COOH* + *$	1.00	0.80	-0.52	-0.59	0.83	0.03
$COOH* + * \leftrightarrows CO_2* + H*$	0.00	1.00	-0.57	0.31	0.95	0.02

Table S9. Parameters and results of linear scaling relationships for energy barriers, $\Delta E_i = a(xE_{CO*} + yE_{OH*}) + b$.

Reaction	x	y	a	b	R^2	MAE
$H_2O(g) + * + * \rightleftharpoons H* + OH*$	0.23	1.00	0.92	0.53	0.87	0.06
$CO* + OH* \rightleftharpoons COOH* + *$	1.00	-1.00	-0.52	-0.69	0.91	0.04
$COOH* + * \rightleftharpoons CO_2* + H*$	1.00	-1.00	0.24	1.14	0.98	0.01

Table S10. Comparison of E_{CO*} and E_{OH*} on Pt(111) and the PtCuPt(111) surface by different density functionals.

Binding energy (eV)	Surface	Density functionals			
		BEEF	PBE	vdw-DF	xPBE
	Pt(111)	-1.46	-1.76	-1.30	-1.54
E_{CO*}	PtCuPt(111)	-1.21	-1.56	-0.99	-1.31
	Difference	0.25	0.20	0.31	0.24
	Pt(111)	0.76	0.75	0.68	0.91
E_{OH*}	PtCuPt(111)	1.13	1.14	1.05	1.25
	Difference	0.37	0.38	0.37	0.34

Table S11. Energetic parameters and kinetic properties of Pt and the PtRePt alloy by DFT calculations and linear scaling relationship.

	Calculating method	Pt	PtRePt
$E_a(RDS)$(eV)	DFT	0.83	0.93
	Linear scaling relationship	0.93	0.67
E_{CO*}(eV)	DFT	-1.46	-1.16
	Linear scaling relationship	-	-
TOF	DFT	1.4×10^{-5}	4.6×10^{-6}
	Linear scaling relationship	1.4×10^{-7}	1.7×10^{-3}

Table S12. Energetic parameters and kinetic properties of different PtCu alloys by DFT calculations.

	$E_a(RDS)$(eV)	E_{CO*}(eV)	TOF
Pt	0.83	-1.46	1.4×10^{-5}
PtCuPt	1.39	-1.21	2.7×10^{-11}
$Cu_1@Pt$	1.02	-1.58	1.7×10^{-10}
$Cu_1@PtCuPt$	1.42	-1.26	4.9×10^{-13}

Table S13. E_{OH*} and E_{CO*} of different Ru$_1$Pt@PtMPt alloys (eV)

	E_{OH*}	E_{CO*}^{Ru}	E_{CO*}^{Pt}	$E_{CO*}^{Ru} - E_{CO*}^{Pt}$
Ru$_1$@PtRuPt	0.06	-1.51	-1.20	-0.31
Ru$_1$@PtAgPt	-0.03	-2.20	-1.40	-0.80
Ru$_1$@PtAuPt	0.06	-2.21	-1.50	-0.71
Ru$_1$@PtCuPt	0.13	-1.99	-1.21	-0.78
Ru$_1$@PtIrPt	0.04	-1.68	-1.12	-0.56
Ru$_1$@PtOsPt	0.00	-1.55	-1.08	-0.47
Ru$_1$@PtPdPt	0.15	-1.92	-1.55	-0.37
Ru$_1$@PtRePt	0.05	-1.34	-1.16	-0.18
Ru$_1$@PtRhPt	0.11	-1.69	-1.17	-0.52

Table S14. Energy barrier of RDS, E_{CO*} and TOF of the Ru promoter on different subsurface metals.

	$E_a(RDS)$(eV)	E_{CO*}^{Ru}(eV)	E_{CO*}^{Pt}(eV)	θ_*	TOF
Ru$_1$@Pt	0.35	-1.87	-1.46	5.67×10^{-5}	3.0×10^{-4}
Ru$_1$@PtRuPt	0.49	-1.51	-1.20	1.14×10^{-6}	5.4×10^{-7}
Ru$_1$@PtOsPt	0.39	-1.55	-1.08	2.06×10^{-8}	1.4×10^{-5}
Ru$_1$@PtRePt	0.62	-1.34	-1.16	1.58×10^{-4}	9.9×10^{-7}

Table S15. Energetic and kinetic parameters of different PtRu alloys.

Alloys	$E_a(RDS)$(eV)	E_{CO*}^{Ru}(eV)	θ_*	TOF
Ru$_1$@Pt	0.34	-1.87	5.67×10^{-6}	3.0×10^{-4}
Ru$_2$@Pt	0.32	-1.85	3.22×10^{-5}	1.3×10^{-3}
Ru$_3$@Pt	0.30	-1.84	1.99×10^{-3}	2.2×10^{-2}
Ru$_{1-1}$@Pt	0.42	-1.70	1.87×10^{-3}	4.3×10^{-3}
Ru$_{1-2}$@Pt	0.45	-1.55	3.32×10^{-2}	8.9×10^{-2}
Ru$_{1-3}$@Pt	0.41	-1.50	1.07×10^{-1}	1.5×10^{0}

Table S16. Formation energies of different PtRu alloys.

Alloys	ΔE(eV)
Ru$_1$@Pt	0.64
Ru$_{0-1}$@Pt	0.03
Ru$_{0-2}$@Pt	0.01
Ru$_{0-3}$@Pt	-0.03
Ru$_2$@Pt	0.64
Ru$_3$@Pt	0.63
Ru$_{1-1}$@Pt	0.28
Ru$_{1-2}$@Pt	0.15
Ru$_{1-3}$@Pt	0.08

Reference

1. Kresse, G.; Furthmuller, J., Efficiency of ab-initio total energy calculations for metals and semiconductors using a plane-wave basis set. *Comput. Mater. Sci.* **1996,** *6*, 15-50.

2. Kresse, G.; Furthmuller, J., Efficient iterative schemes for ab initio total-energy calculations using a plane-wave basis set. *Phys. Rev. B* **1996,** *54*, 11169-11186.

3. Blochl, P. E., Projector augmented-wave method. *Phys. Rev. B* **1994,** *50*, 17953-17979.

4. Kresse, G.; Joubert, D., From ultrasoft pseudopotentials to the projector augmented-wave method. *Phys. Rev. B* **1999,** *59*, 1758-1775.

5. Wellendorff, J.; Lundgaard, K. T.; Møgelhøj, A.; Petzold, V.; Landis, D. D.; Nørskov, J. K.; Bligaard, T.; Jacobsen, K. W., Density functionals for surface science: Exchange-correlation model development with Bayesian error estimation. *Phys. Rev. B* **2012,** *85*, 235149.

6. Perdew, J. P.; Burke, K.; Ernzerhof, M., Generalized gradient approximation made simple. *Phys. Rev. Lett.* **1996,** *77*, 3865-3868.

7. Xu, X.; Goddard, W. A., The extended Perdew-Burke-Ernzerhof functional with improved accuracy for thermodynamic and electronic properties of molecular systems. *J. Chem. Phys.* **2004,** *121*, 4068-4082.

8. Lee, K.; Murray, É. D.; Kong, L.; Lundqvist, B. I.; Langreth, D. C., Higher-accuracy van der Waals density functional. *Phys. Rev. B* **2010,** *82*, 081101.

9. Henkelman, G.; Jonsson, H., A dimer method for finding saddle points on high dimensional potential surfaces using only first derivatives. *J. Chem. Phys.* **1999,** *111*, 7010-7022.

10. Henkelman, G.; Jonsson, H., Improved tangent estimate in the nudged elastic band method for finding minimum energy paths and saddle points. *J. Chem. Phys.* **2000,** *113*, 9978-9985.

11. Henkelman, G.; Uberuaga, B. P.; Jonsson, H., A climbing image nudged elastic band method for finding saddle points and minimum energy paths. *J. Chem. Phys.* **2000,** *113*, 9901-9904.

12. Campbell, C. T.; Sellers, J. R., The entropies of adsorbed molecules. *J. Am. Chem. Soc.* **2012,** *134*, 18109-18115.

13. Data from NIST Standard Reference Database: NIST Chemistry WebBook, http://webbook.nist.gov/chemistry/.

14. Gokhale, A. A.; Kandoi, S.; Greeley, J. P.; Mavrikakis, M.; Dumesic, J. A., Molecular-level descriptions of surface chemistry in kinetic models using density functional theory. *Chem. Eng. Sci.* **2004,** *59*, 4679-4691.

15. Shen, T.; Yang, Y.; Xu, X., Structure-Reactivity Relationship for Nano-Catalysts in the Hydrogenation/Dehydrogenation Controlled Reaction Systems. *Angew. Chem. Int. Ed.* **2021,** *60*, 26342-26345.

16. Gokhale, A. A.; Dumesic, J. A.; Mavrikakis, M., On the mechanism of low-temperature water gas shift reaction on copper. *J. Am. Chem. Soc.* **2007,** *130*, 1402-1414.

17. Williams, W. D.; Greeley, J. P.; Delgass, W. N.; Ribeiro, F. H., Water activation and carbon monoxide coverage effects on maximum rates for low temperature water-gas shift catalysis. *J. Catal.* **2017,** *347*, 197-204.

18. Stamatakis, M.; Chen, Y.; Vlachos, D. G., First-Principles-Based Kinetic Monte Carlo Simulation of the Structure Sensitivity of the Water-Gas Shift Reaction on Platinum Surfaces. *J. Phys. Chem. C* **2011,** *115*, 24750-24762.

19. Yang, L.; Karim, A.; Muckerman, J. T., Density Functional Kinetic Monte Carlo Simulation of Water-Gas Shift Reaction on Cu/ZnO. *J. Phys. Chem. C* **2013,** *117*, 3414-3425.

20. Chen, Z.; Wang, H.; Su, N. Q.; Duan, S.; Shen, T.; Xu, X., Beyond Mean-Field Microkinetics: Toward Accurate and Efficient Theoretical Modeling in Heterogeneous Catalysis. *ACS Catal.* **2018,** *8*, 5816-5826

21. Duke, A. S.; Xie, K.; Brandt, A. J.; Maddumapatabandi, T. D.; Ammal, S. C.; Heyden, A.; Monnier, J. R.; Chen, D. A., Understanding Active Sites in the Water-Gas Shift Reaction for Pt-Re Catalysts on Titania. *ACS Catal.* **2017,** *7*, 2597-2606.

22. Flaherty, D. W.; Yu, W.-Y.; Pozun, Z. D.; Henkelman, G.; Mullins, C. B., Mechanism for the water-gas shift reaction on monofunctional platinum and cause of catalyst deactivation. *J. Catal.* **2011,** *282*, 278-288.

23. Chen, J. F.; Mao, Y.; Wang, H. F.; Hu, P., Reversibility Iteration Method for Understanding Reaction Networks and for Solving Microkinetics in Heterogeneous Catalysis. *ACS Catal.* **2016,** *6*, 7078-7087.

24. Chen, Z.; Wang, H.; Liu, Z. Y.; Xu, X., Dynamic and Intermediate-Specific Local Coverage Controls the Syngas Conversion on Rh(111) Surfaces: An Operando Theoretical Analysis. *ACS Catal.* **2021,** *11*, 3830-3841.

25. Xie, W.; Xu, J.; Ding, Y.; Hu, P., Quantitative Studies of the Key Aspects in Selective Acetylene Hydrogenation on Pd(111) by Microkinetic Modeling with Coverage Effects and Molecular Dynamics. *ACS Catal.* **2021,** *11*, 4094-4106.

26. Guo, C.; Mao, Y.; Yao, Z.; Chen, J.; Hu, P., Examination of the key issues in microkinetics: CO oxidation on Rh(1 1 1). *J. Catal.* **2019,** *379*, 52-59.

27. Xie, W.; Hu, P., Influence of Surface Defects on Activity and Selectivity: A Quantitative Study of Structure Sensitivity of Pd Catalysts for Acetylene Hydrogenation. *Catal. Sci. Technol.*, **2021,** *11*, 5212-5222.

28. Ertl, G.; Neumann, M.; Streit, K. M. Chemisorption of CO on the Pt(111) surface. *Surf. Sci.* **1977**, *64*, 393-410.

29. Feibelman, P. J.; Hammer, B.; Nørskov, J. K.; Wagner, F.; Scheffler, M.; Stumpf, R.; Watwe, R.; Dumesic, J. The CO/Pt(111) Puzzle. *J. Phys. Chem. B* **2001**, *105*, 4018-4025.

30. Kugai, J.; Miller, J. T.; Guo, N.; Song, C. S., Oxygen-enhanced water gas shift on ceria-supported Pd-Cu and Pt-Cu bimetallic catalysts. *J. Catal.* **2011,** *277*, 46-53.

31. Rao, K. K.; Do, Q. K.; Pham, K.; Maiti, D.; Grabow, L. C., Extendable Machine Learning Model for the Stability of Single Atom Alloys. *Top. Catal.* **2020,** *63*, 728-741.